DEVELOPMENT OF A CODE FOR THE SIMULATION OF AEROACOUSTIC PHENOMENA IN A MIXING LAYER

Alysson Kennerly Colaciti, alysson@sc.usp.br
USP - Universidade de São Paulo, NPA - SMM - EESC. Av. Trabalhador Sãocarlense, 400, Centro, cep:13560-970, São Carlos - SP Brasil.

Jörn Sesterhenn, joern.sesterhenn@alumni.ethz.ch
Universität der Bundeswehr München.

Ricardo A. Coppola Germanos, gercop@sc.usp.br
Marcello Augusto Faraco de Medeiros, marcello@sc.usp.br
USP - Universidade de São Paulo, NPA - SMM - EESC. Av. Trabalhador Sãocarlense, 400, Centro, cep:13560-970, São Carlos - SP Brasil.

Abstract. *The aim of the present work is to develop a code to investigate numerically the aeroacoustic phenomena in a mixing layer under temporal development. Direct numerical simulation with high accuracy finite difference scheme was chosen. The mesh employed in the present work was stretched in y-direction to provide a better resolution in the vortical region of the mixing layer. The stretching influence on the accuracy has been also investigated. A filtering scheme was tested and later used to produce the final results of the present work. A characteristic-type formulation of the compressible 2D Navier Stokes equations was used. For time development of the mixing layer it is necessary to adopt periodic boundary condition in x-direction, what makes it more difficult to reproduce a single vortex pairing inside a wide domain. The chosen domain was large enough to provide a clear observation of the acoustic field produced by the pairing. The Mach number has been varied to observe it's influence on the acoustic field.*

Keywords: *Aeroacoustics, Vortex pairing, Flow instability, Mixing layer, DNS*

1. Introduction

The aim of the present work is to develop a code to investigate the acoustic phenomena in a 2D mixing layer by Direct Numerical Simulation of the compressible Navier-Stokes equations. Flow generated sound is a serious problem in many engineering applications. It can cause human discomfort; it affects the stealth operation of military vehicles; etc. Due to the current aircraft traffic, community noise concerns at busy airports constraint the operation of noisy aircraft. In response to this fact, FAA also included stringent regulations to the aircraft noise level operation and certification [Want et al. (2006); Colonius and Lele (2004)]. Airframe noise is the major responsible for the sound level of landing aircraft, since the propulsion system is near to the lowest power level. The impact of those mentioned facts on the worldwide aircraft industry is the greater attention paid to noise in the design stage, leading to the needs of efficient noise level prediction methods.

Flow instability phenomena are determinant to a wide range of aerodynamically generated sound. This strong link is due to the transient and periodic nature of both the flow instability and the aerodynamic sound generation phenomena. Two classical cases of aerodynamic sound generation are the vortex-shedding and vortex pairing [Want et al. (2006); Colonius and Lele (2004)]. The vortex pairing phenomenon has been mostly observed in the mixing layer flow case. The vortex pairing phenomenon follows a chain of events starting with the primary disturbance amplification leading to the production of vortex structures, which is the classical Kelvin Helmholtz instability mechanism. Those small primary disturbances exponentially grow in time or space and reach the saturation point, when the vortex structures are formed. Thus, when the vortex distribution geometry is already established, the secondary instability takes place leading to the pairing of the primary vortices.

In numerical simulations of sound generation, Colonius et al. (1997); Colonius and Lele (2004); showed typical discrepancies between the disturbances near the vortical region and the acoustic disturbances at the far field region. The acoustic disturbances were 4 or even 5 orders of magnitude lower. This shows that the code accuracy is strongly relevant for aeroacoustic study purposes. A code developed by Germanos and Medeiros (2005) was used to investigate the flow instability of a compressible shear layer. The code accuracy was an important concern in their work. They used a high order compact finite difference scheme to compute the spatial derivatives and a 4^{th} order Runge-Kutta scheme for the time integration. Germanos and Medeiros (2005) verified the code against the Linear Stability Theory (LST).

A double spiral pattern of the far-field pressure was observed by Mitchell et al. (1995) by Direct Numerical Simulation (DNS) of the compressible Navier Stokes equations of a co-rotating vortex pairing. The formulation considered an isentropic process and the results were compared with acoustic analogies proposed by [Powell (1964), Möhring (1978, 1979) and Lighthill (1952)]. The same double spiral structure, corresponding to the rotation of a quadrupole source type

was obtained by Large Eddy Simulations (LES) of a free shear layer under spatial development in Bogey et al. (2000). Colaciti et al. (2006) shows by DNS of a mixing layer under temporal development similar acoustic behavior caused by the vortex pairing. Bogey, et. al. attributed this rotation of the quadrupoles sources to the rollup of the two co-rotative vortices, i.e., the rotation of the vortex structures during the pairing.

For a low Ma number regime, there is a great discrepancy between the characteristic lengths of acoustic and vortex scales [Colonius et al. (1997), Bogey et al. (2000) and Colaciti et al. (2006)]. Likewise, to combine a high resolution both in the vortical region, the acoustic region (far-field) and a simulation at affordable computational cost, a stretched mesh was used. To verify the use and implementation of such a technique, the accuracy of the spatial derivative computation in a stretched mesh was investigated and the order of the scheme was found to be constant.

Non reflecting boundary conditions is one of the hardest challenge in the development of a CFD code, in particular, for investigative aeroacoustic purposes, in which one is usually interested in the behavior of acoustic waves propagating in an infinite domain. A commonly used strategy to prevent spurious acoustic wave reflections consists in increasing the domain size with a sponge zone near the boundaries. Such technique has been proved to be inefficient, as incrementing the domain size rapidly increases the computational cost. A characteristic-type formulation of the compressible Navier-Stokes equation (Sesterhenn (2001)) has been successfully adopted in Colaciti et al. (2006). It has been shown, in Colaciti et al. (2006), for a 1D domain, to have a reflection rate below 0.08%. In the current work the same characteristic-type formulation and anechoic boundary mimicking technique was adopted.

The use of filtering schemes is very common in direct numerical simulations. The fact is that, in some cases, the influence of very small scales (dissipative scales) are of no interest, and, a grosser mesh can be used. Filtering schemes are necessary in such situations to prevent aliasing problems. In the present work different variables were filtered, analyzed, and a set of variables was proposed to be filtered on the simulation of shear flows. This set appears to exhibit a better performance than other more commonly used sets. The reason for the choice of the filtered variables proposed on the current work is strongly linked to the Gibbs phenomenon and is better explained on the following sections.

2. Methodology

In the present section it is given a brief explanation of the techniques used in the current work.

2.1 Formulation

The formulation adopted in the present work consists in the same formulation proposed in Sesterhenn (2001). The set of variables used in this formulation are: p (pressure), u (x-direction velocity), v (y-direction velocity), w (z-direction velocity), s (entropy). One of the advantages of using the characteristics-type formulation of the compressible Navier-Stokes equations is an easier implementation of the non reflecting boundary conditions. With the aid of the present formulation the useful domain is identical to the computational domain and no sponge zone is necessary to provide simulations without significant spurious reflections on the boundaries. An full description of the variables used on the characteristic-type formulation can be seen in Sesterhenn (2001) and Colaciti et al. (2006). For brevity, the 3D set of equations will be only shown below:

$$\begin{aligned}
\frac{\partial p}{\partial t} &= -\frac{\rho c}{2}\left[\left(X^{+}+X^{-}\right)+\left(Y^{+}+Y^{-}\right)+\left(Z^{+}+Z^{-}\right)\right]+\frac{p}{c_v}\left(\frac{\partial s}{\partial t}+X^{s}+Y^{s}+Z^{s}\right)\\
\frac{\partial u}{\partial t} &= -\left[\frac{1}{2}\left(X^{+}-X^{-}\right)+Y^{u}+Z^{u}\right]+\frac{1}{\rho}\frac{\partial \tau_{1j}}{\partial x_j}\\
\frac{\partial v}{\partial t} &= -\left[X^{v}+\frac{1}{2}\left(Y^{+}-Y^{-}\right)+Z^{v}\right]+\frac{1}{\rho}\frac{\partial \tau_{2j}}{\partial x_j}\\
\frac{\partial w}{\partial t} &= -\left[X^{w}+Y^{w}+\frac{1}{2}\left(Z^{+}-Z^{-}\right)\right]+\frac{1}{\rho}\frac{\partial \tau_{3j}}{\partial x_j}\\
\frac{\partial s}{\partial t} &= -\left(X^{s}+Y^{s}+Z^{s}\right)+\frac{R}{p}\left(-\frac{\partial q_i}{\partial x_i}+\phi\right).
\end{aligned} \tag{1}$$

With the wave terms, heat transfer term, viscous term and viscous dissipation term defined as follows:

$$X^{+}=(u+c)\left(\frac{1}{\rho c}\frac{\partial p}{\partial x}+\frac{\partial u}{\partial x}\right); \qquad X^{-}=(u-c)\left(\frac{1}{\rho c}\frac{\partial p}{\partial x}-\frac{\partial u}{\partial x}\right);$$

$$X^{v}=u\frac{\partial v}{\partial x}; \qquad X^{w}=u\frac{\partial w}{\partial x}; \qquad X^{s}=u\frac{\partial s}{\partial x};$$

$$Y^+ = (v+c)\left(\frac{1}{\rho c}\frac{\partial p}{\partial y} + \frac{\partial v}{\partial y}\right); \qquad Y^- = (v-c)\left(\frac{1}{\rho c}\frac{\partial p}{\partial y} - \frac{\partial v}{\partial y}\right);$$

$$Y^u = v\frac{\partial u}{\partial y}; \qquad Y^w = v\frac{\partial w}{\partial y}; \qquad Y^s = v\frac{\partial s}{\partial y};$$

$$Z^+ = (w+c)\left(\frac{1}{\rho c}\frac{\partial p}{\partial z} + \frac{\partial w}{\partial z}\right); \qquad Z^- = (w-c)\left(\frac{1}{\rho c}\frac{\partial p}{\partial z} - \frac{\partial w}{\partial z}\right);$$

$$Z^u = w\frac{\partial u}{\partial z}; \qquad Z^v = w\frac{\partial v}{\partial z}; \qquad Z^s = w\frac{\partial s}{\partial z};$$

$$\tau_{ij} = \mu\left[\frac{\partial u_j}{\partial x_i} + \frac{\partial u_i}{\partial x_j} - \frac{2}{3}\left(\nabla\vec{V}\right)\delta_{ij}\right];$$

$$q_i = -\lambda\frac{\partial T}{\partial x_i};$$

$$\phi = \tau ij E_{ij};$$

$$E_{ij} = \frac{1}{2}\left(\frac{\partial u_i}{\partial x_j} + \frac{\partial u_j}{\partial x_i}\right).$$

2.2 Numerical scheme

The numerical scheme adopted performs time-integration with a 4^{th} order Runge-Kutta scheme. Computation of the spatial derivatives were done in each pseudo time step of the Runge-Kutta scheme. To prevent aliasing problems some of the state variables (p and w) are filtered in the last pseudo time step of the Runge-Kutta scheme and the remaining ones ($\frac{\partial u}{\partial t}$, $\frac{\partial v}{\partial t}$ and $\frac{\partial s}{\partial t}$) are filtered in each pseudo time step of the Runge-Kutta scheme. The reason for the choice of each variable to be directly filtered or to be filtered by filtering it's temporal derivative is shown in sec. (2.2.2).

2.2.1 Spatial derivatives

Spatial derivatives were calculated with a high order compact finite difference scheme, as proposed by Lele (1992). For the first and second derivatives a centered scheme with 3 points on the left-hand-side stencil and 5 points on the right-hand-side were adopted for the medium points. The set of difference equations were solved by a tri-diagonal matrix solver. The numerical scheme adopted for the first derivative was, in matrix form:

$$\begin{pmatrix}
1 & 7 & 0 & & & & & & \\
1 & 10 & 10 & 0 & & & & 0 & \\
0 & 1 & 3 & 1 & 0 & & & & \\
 & 0 & 1 & 3 & 1 & 0 & & & \\
 & & & \ddots & \ddots & \ddots & & & \\
 & & & 0 & 1 & 3 & 1 & 0 & \\
 & & & & 0 & 1 & 3 & 1 & 0 \\
 & 0 & & & & 0 & 10 & 10 & 1 \\
 & & & & & & 0 & 7 & 1
\end{pmatrix} \cdot \begin{pmatrix} f'_1 \\ f'_2 \\ f'_3 \\ f'_4 \\ \vdots \\ f'_{n-3} \\ f'_{n-2} \\ f'_{n-1} \\ f'_n \end{pmatrix} = \begin{pmatrix} b_1 \\ b_2 \\ b_3 \\ b_4 \\ \vdots \\ b_{n-3} \\ b_{n-2} \\ b_{n-1} \\ b_n \end{pmatrix}$$

where:

$$b_1 = \frac{-3.5929f_1 - 3.15f_2 + 10.5f_3 - 5.8333f_4 + 2.9167f_5 - 1.05f_6 + 0.2333f_7 - 0.0238f_8}{\delta x};$$

$$b_2 = \frac{-3.7833f_1 - 10.8333f_2 + 11.6667f_3 + 3.3333f_4 - 0.4167f_5 + 0.0333f_6}{\delta x};$$

for the medium points ($3 < i < n-2$):

$$b_i = \frac{-0.0833f_{i-2} - 2.3333f_{i-1} + 2.3333f_{i+1} + 0.0833f_{i+2}}{\delta x}$$

$$b_{n-1} = \frac{+3.7833f_n + 10.8333f_{n-1} - 11.66667f_{n-2} - 3.3333f_{n-3} + 0.4167f_{n-4} - 0.0333f_{n-5}}{\delta x};$$

$$b_n = \frac{+3.5929f_n + 3.15f_{n-1} - 10.5f_{n-2} + 5.8333f_{n-3} - 2.9167f_{n-4} + 1.05f_{n-5} - 0.2333f_{n-6} + 0.0238f_{n-7}}{\delta x}.$$

The numerical scheme adopted for the second derivative was:

$$\begin{pmatrix} 1 & 13.6502 & 0 & & & & & & \\ 1 & 122.4 & 610.2 & 0 & & & & 0 & \\ 0 & 1 & 5.5 & 1 & 0 & & & & \\ & 0 & 1 & 5.5 & 1 & 0 & & & \\ & & & \ddots & \ddots & \ddots & & & \\ & & & 0 & 1 & 5.5 & 1 & 0 & \\ & & & & 0 & 1 & 5.5 & 1 & 0 \\ & 0 & & & & 0 & 610.2 & 122.4 & 1 \\ & & & & & & 0 & 13.6502 & 1 \end{pmatrix} \cdot \begin{pmatrix} f_1'' \\ f_2'' \\ f_3'' \\ f_4'' \\ \vdots \\ f_{n-3}'' \\ f_{n-2}'' \\ f_{n-1}'' \\ f_n'' \end{pmatrix} = \begin{pmatrix} b_1 \\ b_2 \\ b_3 \\ b_4 \\ \vdots \\ b_{n-3} \\ b_{n-2} \\ b_{n-1} \\ b_n \end{pmatrix}$$

where:

$$b_1 = \frac{14.708f_1 - 27.139f_2 + 5.452f_3 + 15.40f_4 - 13.916f_5 + 7.756f_6 - 2.807f_7 + 0.604f_8 - 0.059f_9}{\delta x};$$

$$b_2 = \frac{53.6011f_1 + 655.56f_2 - 1567.95f_3 + 969.3778f_4 - 126.45f_5 + 17.16f_6 - 1.2989f_7}{\delta x};$$

for the medium points ($3 < i < n-2$):

$$b_i = \frac{0.375f_{i-2} + 6f_{i-1} - 12.75f_i + 6f_{i+1} + 0.375f_{i+2}}{\delta x}$$

$$b_{n-1} = \frac{53.6011f_n + 655.56f_{n-1} - 1567.95f_{n-2} + 969.3778f_{n-3} - 126.45f_{n-4} + 17.16f_{n-5} - 1.2989f_{n-6}}{\delta x};$$

$$b_n = \frac{14.708f_n - 27.139f_{n-1} + 5.452f_{n-2} + 15.40f_{n-3} - 13.916f_{n-4} + 7.756f_{n-5} - 2.807f_{n-6} + 0.604f_{n-7} - 0.059f_{n-8}}{\delta x}.$$

A mesh stretched in the y-direction was used in the present work. The computation of spatial derivatives by compact schemes were carried out in an uniform grid. A coordinate transformation was then used to obtain the derivatives in the stretched mesh. The transformation used is given by Anderson (1990):

$$\begin{aligned} y_p &= B + \frac{1}{\tau}\sinh^{-1}\left[\left(\frac{y_c}{y_{\text{center}}} - 1\right)\sinh(\tau B)\right], \\ B &= \frac{1}{2\tau}\ln\left[\frac{1 + (e^{\tau} - 1)\left(\frac{y_{\text{center}}}{h}\right)}{1 + (e^{-\tau} - 1)\left(\frac{y_{\text{center}}}{h}\right)}\right], \end{aligned} \tag{2}$$

where y_p is the physical y-coordinate, y_c is the computational y-coordinate ($0 < y_c < 1$), y_{center} is the y-coordinate in the physical domain where the mesh points are agglomerated, h is the height of the y-range in the physical domain and τ is the stretching parameter. An example of a typical stretched mesh can be seen in Fig.1.

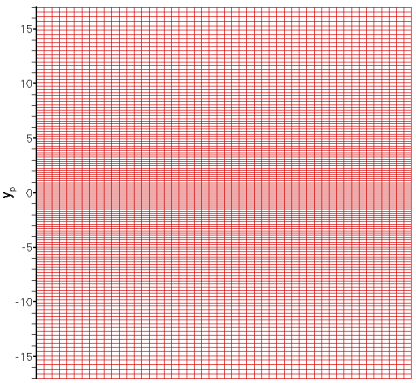

Figure 1. Stretched mesh with $\tau = 3$, $h = 34$ and $y_{\text{center}} = 0$.

Actually, for the y-direction, the spatial derivative scheme firstly computes the derivative of a function with respect to the computational frame, i.e., in a mesh with constant $\delta y_c = \frac{1}{n-1}$ where n is the number of points and δy_c the mesh

spacing in the computational domain. A metric multiplication must then be done to get the derivatives in the physical domain.

$$\begin{aligned}\frac{\partial u}{\partial y_p} &= \frac{\partial u}{\partial y_c}\underbrace{\frac{\partial y_c}{\partial y_p}}_{\text{metric}}; \\ \frac{\partial^2 u}{\partial y_p^2} &= \frac{\partial^2 u}{\partial y_c^2}\underbrace{\left(\frac{\partial y_c}{\partial y_p}\right)^2}_{\text{metric}} + \frac{\partial u}{\partial y_c}\underbrace{\frac{\partial^2 y_c}{\partial y_p^2}}_{\text{metric}};\end{aligned} \tag{3}$$

Once it is not possible to display the derivatives $\frac{\partial y_c}{\partial y_p}$ and $\frac{\partial^2 y_c}{\partial y_p^2}$ and it is possible to find $\frac{\partial y_p}{\partial y_c}$ and $\frac{\partial^2 y_p}{\partial y_c^2}$, then eqs. (3) must be expressed as functions of $\frac{\partial y_p}{\partial y_c}$ and $\frac{\partial^2 y_p}{\partial y_c^2}$. In the current work, the values of such derivatives were obtained by the numerical scheme presented at the begin of this section. Defining the following functions and assuming that both are bijective:

$$y_c = f(y_p), \tag{4}$$

$$y_p = f^{-1}(y_c) = g(y_c), \tag{5}$$

therefore:

$$g(f(y_p)) = y_p. \tag{6}$$

Now taking the derivative of eq. (6) with respect to y_p and recalling eqs. (4) and (5) and using the chain rule:

$$\begin{aligned}\frac{\partial [g]}{\partial y_p}(f(y_p))\frac{\partial [f]}{\partial y_p}(y_p) &= 1, \\ \Rightarrow \frac{\partial [g]}{\partial y_p}(y_c)\frac{\partial [f]}{\partial y_p}(y_p) &= 1, \\ \Rightarrow g'(y_c) f'(y_p) &= 1, \\ \Rightarrow \frac{\partial y_c}{\partial y_p} = f'(y_p) = \frac{1}{g'(y_c)} &= \frac{1}{\frac{\partial y_p}{\partial y_c}}.\end{aligned} \tag{7}$$

Now deriving eq. (7) with respect to y_p:

$$\frac{\partial^2 y_c}{\partial y_p^2} = f''(y_p)\frac{\partial y_p}{\partial y_p} = \frac{-1}{[g'(y_c)]^2} g''(y_c)\frac{\partial y_c}{\partial y_p} = \frac{-\frac{\partial^2 y_p}{\partial y_c^2}}{\left(\frac{\partial y_p}{\partial y_c}\right)^3}. \tag{8}$$

Now, with eqs. (7) and (8) it is possible to perform the full transformation:

$$\begin{aligned}\frac{\partial u}{\partial y_p} &= \frac{\partial u}{\partial y_c}\underbrace{\frac{1}{\frac{\partial y_c}{\partial y_p}}}_{\text{metric}}, \\ \frac{\partial^2 u}{\partial y_p^2} &= \frac{\partial^2 u}{\partial y_c^2}\underbrace{\left(\frac{1}{\frac{\partial y_p}{\partial y_c}}\right)^2}_{\text{metric}} + \frac{\partial u}{\partial y_c}\underbrace{\frac{\frac{\partial^2 y_p}{\partial y_c^2}}{\left(\frac{\partial y_p}{\partial y_c}\right)^3}}_{\text{metric}}.\end{aligned} \tag{9}$$

One may point out a clear fact that as the grid is stretched the error at the center reduces and increases at the border.

Herein and after, y must be interpreted as the y-coordinate in the physical domain (y_p, previously). Tests were performed to verify the spatial derivative scheme in a stretched mesh. In these tests a y-domain ranging from $-1 < y < 1$

was used to compute the first and second derivatives of the function $u(y) = \tanh(5y)$. This function is similar to the velocity profile used to study mixing layers. The numerical scheme firstly computes $\frac{\partial u}{\partial y_c}$ and $\frac{\partial^2 u}{\partial y_c^2}$. Then metrics ($\frac{\partial y_p}{\partial y_c}$ and $\frac{\partial^2 y_p}{\partial y_c^2}$) are numerically computed and used in eqs. (9) to give $\frac{\partial u}{\partial y}$ and $\frac{\partial^2 u}{\partial y^2}$. Fig. 2 shows the maximum absolute error for the first and second derivatives as a function of mesh refinement. For each mesh case $\delta y = \frac{1}{n-1}$, where n is the number of points used in the computational mesh. One may observe that for the computation of the first derivative, by increasing the stretching parameter from 1.5 to 5.0, for the same number of points, the maximum absolute error reduces about 1 decade. For the second derivative an equal change in the stretching parameter could reduce almost 3 decades in the error.

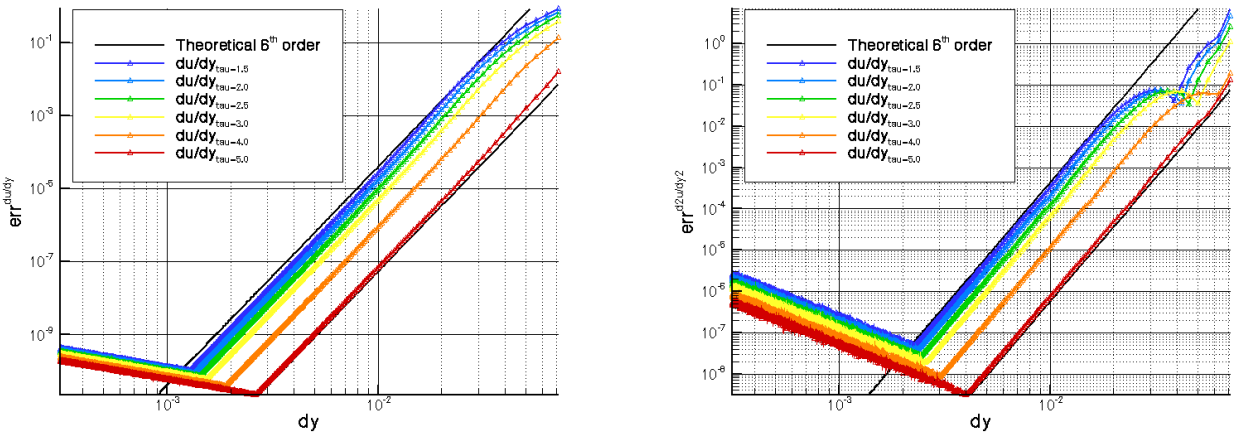

(a) First derivative

(b) Second derivative

Figure 2. Maximum of absolute error versus computational-grid spacing for different stretching parameter values.

2.2.2 Filter

The present work focus the instability of a parallel shear flow. Parallel shear flows have velocity profile (say $u(y)$) generally represented by functions such as hyperbolic tangent, error profile or similar for mixing layers; Gaussian profile or similar for jets and wakes; and so on. Like known, those listed pattern functions have a broad-band spectrum. It is known that the filtering scheme works like a low-pass filter to damp the aliasing. Due to those mentioned facts, one might relate the deforming influence of the filter onto those velocity profiles. Such influence is caused by a phenomenon similar to the Gibbs' phenomenon, where the cut-off frequency will cause an overshoot near to the high curvature regions. Tests were done showing such behavior.

Fig. 3(a) shows the contourplot of function $u(y)_i$ against y and i axis, where i is the number of iterations. $u(y)_i$ was obtained by iterating the initial $u(y)_0 = \tanh(2y)$ profile with a filtering scheme. Fig. 3(b) shows the functions $u(y)_0 = \tanh(2y)$ and $u(y)_{45000}$. The distortion observed in fig. 3(b) varies with the mesh refinement and the number of iterations. As δy increases, the number of iterations necessary to achieve a given distortion will also augment. The filtering schemes was based on the iteration of a 4-th order penta-diagonal scheme proposed by Lele (1992) (C.2.10.b). For the tests performed in the present work a uniform mesh with 129 points was adopted in a domain: $-5 < y < 5$.

Deformations of the velocity profile caused by the filtering scheme may play a strong influence on studies of flow instability. For example, the Kelvin-Helmholtz instability, mostly studied for mixing layers, is known to be strongly influenced by the vorticity thickness. The vorticity thickness itself could be deformed by the filtering scheme during the simulation. Due to those facts, in the current work a criterion was proposed to set the filtering scheme up. For those state variables which have a broad-band spectrum at the initial condition, it should be better to filter it's time-derivative. For the remaining ones, the own variable could be filtered.

3. Code testing

In the present section, results of tests for the verification of the code developed in the current work are shown. The code was used to reproduce the linear stability theory of the Kelvin-Helmholtz type. This is often considered an important technique for code testing [Fortune (2000), Colaciti et al. (2006)]. Fig. 4 shows a sketch of the mixing layer problem.

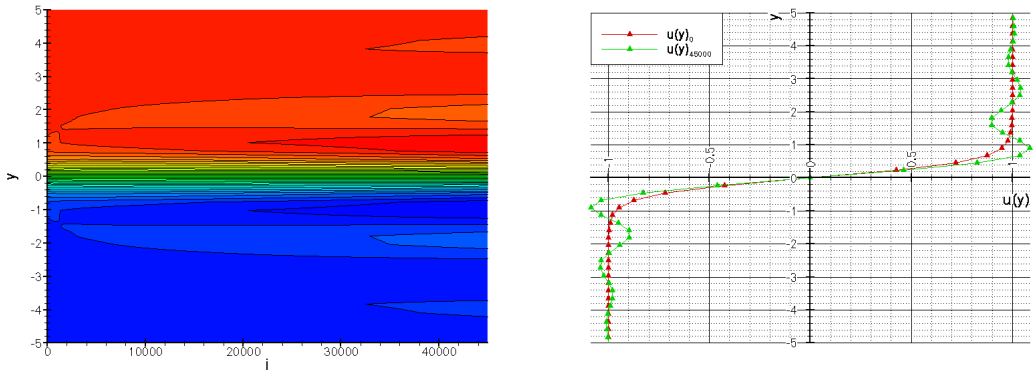

(a) (b)

Figure 3. The contourplot of the result obtained by filtering $u(y)$ and the comparisons between $u(y)$ obtained after filtering 45000 times and the initial $u(y) = \tanh(2y)$ are shown respectively. In fig. 3(b) the red line represents the function $u(y) = \tanh(2y)$ and the green line represents $u(y)$ obtained after filtering 45000 times

The non-dimensional scheme adopted in the present work uses U^*_{max} as the reference velocity, δ^*_w as the reference length, where δ^*_w is defined as the vorticity thickness, ρ^*_∞ as the reference density, $\rho^*_\infty {U^*}^2_{max}$ as the reference pressure, T^*_∞ as the reference temperature and c^*_p as the reference entropy. Time is non-dimensionalized by $\frac{\delta^*_w}{U^*_{max}}$. The simulation adopted a periodic boundary conditions in x-direction and a free-slip anechoic boundary condition [Colaciti et al. (2006), Sesterhenn (2001)].

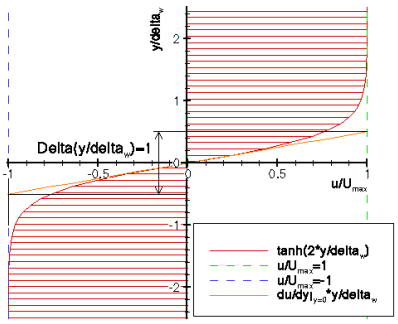

Figure 4. Mixing layer setup.

For the tests shown in the current work, the problem set-up was

$$\delta^*_w = 1; \qquad c^*_\infty = 340.21; \qquad Ma = 0.4; \qquad U^*_{max} = c^*_\infty Ma; \qquad Re = \frac{\rho^* U^*_{max} \delta^*_w}{\mu^*} = 10^5;$$

$$u(x, y, t = 0) = U(y) + u_p(x, y); \qquad U(y) = \tanh(2y); \qquad v(x, y, t = 0) = v_p(x, y);$$

$$T(x, y, t = 0) = 1 - Ma^2 \frac{\gamma - 1}{2} \left(U(y)^2 - 1\right);$$

where the star indicate dimensional variables, $U(y)$ is the base flow, and $u_p(x, y)$ and $v_p(x, y)$ are disturbances of the velocity components in x and y directions, respectively. The initial condition for the vertical velocity disturbances are given by:

$$v_p(x, y) = e^{-\sigma(y)^2} \left[A_0 \cos(\alpha x)\right].$$

By assuming the disturbance field as incompressible, i.e., $\frac{\partial u_p}{\partial x} + \frac{\partial v_p}{\partial y} = 0$, an appropriate u_p disturbance field could be obtained.

The linear stability theory gives the growth rate of an infinitesimal disturbance for a Reynolds number flow. Because of the viscous thickening of the mixing layer base flow the Reynolds number normally varies during the simulation and prevents proper amplification with the theory. However, source terms can be added to the equations in order to avoid this effect, these terms were

- $-\frac{1}{\rho Re}\frac{\partial^2 \bar{u}}{\partial y^2}$;
- $-\frac{\gamma-1}{Re}\left(\frac{\partial \bar{u}}{\partial y}\right)^2$ on the computation of the viscous dissipation ϕ.
- $-\lambda\frac{\partial^2 \bar{T}}{\partial y^2}$ on the computation of the heat exchange $\frac{\partial q_i}{\partial x_i}$.

For both cases, the bar superscript indicates the mean value of velocity (u) or temperature (T) in x direction.

Fig. 8 shows the power spectrum evolution obtained by the first mode of the Fast Fourier Transform of $v(x,0,t)$ in x-direction. Three different wavenumbers, $\alpha = 0.4$, $\alpha = 0.8$ and $\alpha = 1.75$ are shown. This figure shows the linear region and the non-linear region of the disturbance growth. Theoretical results obtained by Sandham (1990) are also ploted in fig.8 for each one of the wavenumbers. Fig.9 shows the disturbance amplification rate (ω_i) for a given disturbance wavenumber (α). Such amplification rate was obtained by performing an exponential fit curve to the evolution of the curves presented in fig. 8. The results presented by Sandham (1990) were obtained by solving the Rayley equations for $Ma = 0.4$. Sandham (1990) also shown that for $Re \geq 10^5$ the amplification rate of the most amplified inviscid eigenfunction matches the inviscid theory to within 0.1%.

Observations of the time development of the $v(x,0,t)$ first mode in x-direction are not enough to perform such analysis. This is necessary to ensure that the first mode will be the main growing mode. Likewise, a difference limit of 2 orders of magnitude between the first mode and the harmonic modes was ensured to determine the measurement of the growth-rate for the **linear** region. Figs. 5, 6 and 7 show the time development of logarithm of the fundamental and harmonics wavenumbers power spectrum $\log\left[\left(A_{Rn}^2 + A_{In}^2\right)^{0.5}\right]$ for the fundamental wavenumbers $\alpha = 0.4$, $\alpha = 0.8$ and $\alpha = 1.75$ respectively, where n represents the $n-1$-th harmonic coefficients, I is the imaginary part and R the real part. One can establish a limit of the ratio between the fundamental and the first-harmonic power spectra $\left(A_{R1}^2 + A_{I1}^2\right)^{0.5} / \left(A_{R2}^2 + A_{I2}^2\right)^{0.5} > 10^{-2}$ to ensure that the simulation is still in the linear growth region. For the case of fundamental wavenumber $\alpha = 0.4$, fig. 5, the simulation can be considered in the linear region up to $t = 60$. For the case $\alpha = 0.8$, fig. 6, such time limit is $t = 50$. For $\alpha = 1.75$, fig. 7, the disturbance growth rate is so small that the power spectrum of the first harmonic does not exceeded 10^{-5} of the fundamental wavenumber power spectrum during the simulation time.

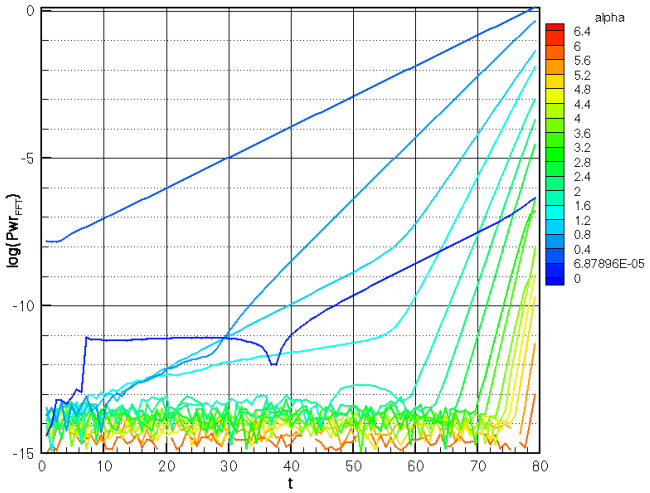

Figure 5. Time development of the fundamental and harmonics wavenumbers power spectrum are shown for the fundamental wavenumber $\alpha = 0.4$.

The mesh adopted here to solve all of the cases had 33 points x-wise and 129 points y-wise. Also the mesh was stretched in y-direction following eqs. (2) with $\tau = 1.8$. For all of the cases the domain was $0 < x < 2\pi/\alpha$; $-17 < y < 17$. Fig. 9 shows a good agreement between simulation and theory and the code was considered adequate for further studies.

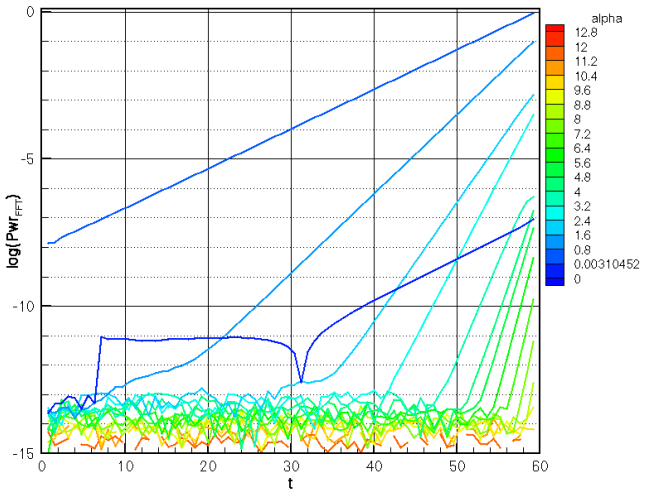

Figure 6. Time development of the fundamental and harmonics wavenumbers power spectrum are shown for the fundamental wavenumber $\alpha = 0.8$.

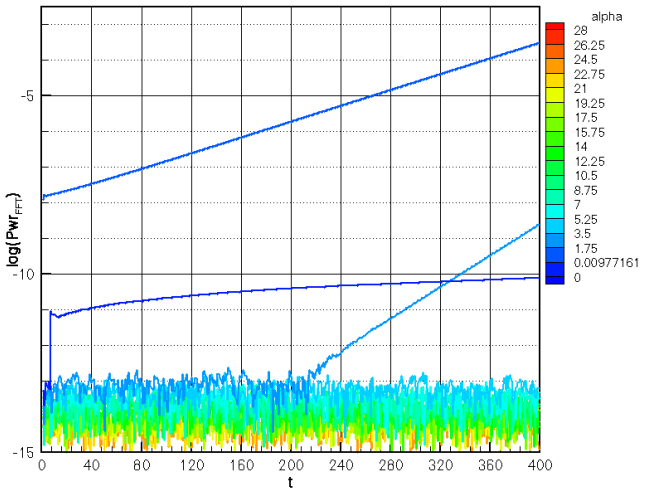

Figure 7. Time development of the fundamental and harmonics wavenumbers power spectrum are shown for the fundamental wavenumber $\alpha = 1.75$.

4. Results

In this section results of the aeroacoustic phenomena are shown and briefly discussed. since the acoustic quantities are very small when compared to the inertial quantities, to analyze such phenomena it is necessary to observe a physical quantity with a resolution of 4 or 5 orders of magnitude [Colonius et al. (1997), Colonius and Lele (2004)]. Therefore $\log$ scale is necessary.

A mesh with 501 points in x-direction, 601 points in y-direction was stretched in y-direction with $\tau = 5$, $-100 < y < 100$, $y_{\text{center}} = 0$, $0 < x < 300$ and used to investigate the aeroacoustic phenomena in mixing layers under temporal development. The investigations were done for three different flow conditions: $Ma = 0.2$, $Ma = 0.4$ and $Ma = 0.6$. The others parameters were kept constant, such as: $\delta_w^* = 1$; $Re = 10^5$; $\Delta t^* = 0.02\frac{\delta_w^*}{U_\infty^*}$. The free-slip anechoic boundary condition [Colaciti et al. (2006), Sesterhenn (2001)] was adopted in the y-direction and the periodic one in x-direction. The flow disturbance was computed with wavepackets following Colaciti et al. (2006).

For different flow conditions a different type of vortex pairing geometry may occur in different non-dimensional time instant values. To synchronize the different flow cases in a common phenomenon stages, a vortex pairing geometry parameter which measures a shear thickness quantity ($\delta_w = 2/\frac{\partial u}{\partial y}$) was evaluated. The idea was to ensure that this parameter was similar for the different simulations. Figs. (10), (11) and (12) were generated by compounding a shaded view of the $\log\left(\frac{P}{P_0}\right)$ with a contour plot of the vorticity field. Through that figures it is possible to observe the far-field, the near field and the vortices structures.

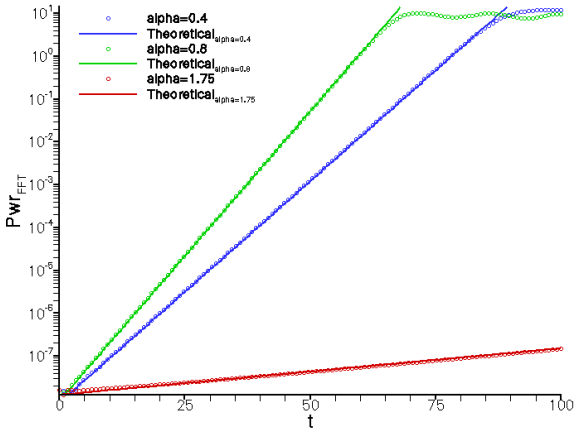

Figure 8. The power spectrum of the given wavenumbers versus time t are shown for $\alpha = 0.4$, $\alpha = 0.8$ and $\alpha = 1.75$ at $Ma = 0.4$. The theoretical results obtained by Sandham (1990) are also shown for comparison purposes. It is possible to observe a linear growth region before the disturbances reach the saturation (non-linear region).

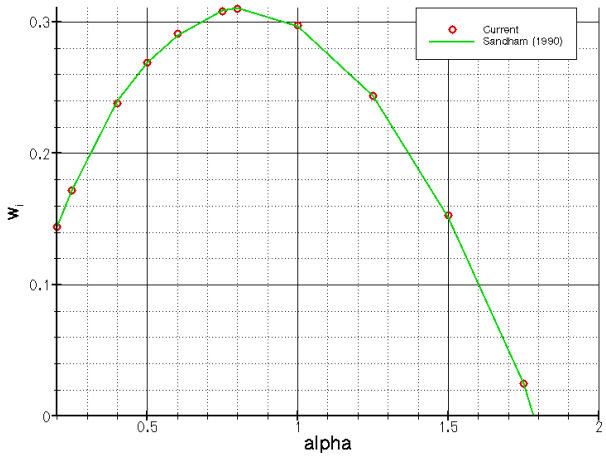

Figure 9. Amplification rate of the disturbances (eigenfunctions) versus wavenumber at $Ma = 0.4$. The green line represents results obtained by Sandham (1990) by solving the Rayleigh equations. The red points represents results obtained in the current work by DNS of the compressible Navier-Stokes equations.

The acoustic wave propagation in shear flows involves some known phenomena such as refraction. The refraction is responsible for the changes in the sound-wave propagation. Through figs. (10), (11) and (12) it is possible to observe that phenomenon. Observe that for $Ma = 0.6$, in fig. (12), the flow reaches a condition in which refracted waves become Mach waves. This is due to the relative speed between the opposite currents, which is 1.2 times the speed of sound. In this case, the upper layer would observe a moving source with a relative speed of 1.2 times the sound speed, reproducing the typical cases in which Mach waves are present. Figs. (10(a)), (11(a)) and (12(a)) show a dark structures similar to that associated with quadrupole acoustic sources. Through the sequences of figs. (10(b)), (10(c)) and (10(d)); and (11(b)), (11(c)) and (11(d)), one observe a rotating quadrupole source-type as reported by Boogey et al. (2000), Mitchell et al. (1995) and Colaciti et al. (2006). For the case of $Ma = 0.6$ it is not possible to do such analysis. The refraction caused by the velocity difference of the currents distort the typical rotating quadrupole structure.

In contrast to simulations which use sponge zones or buffer zones to inhibit spurious acoustic wave reflections, one might observe that, using the characteristic-type formulation, the simulation domain is equal to the full observed domain. Spurious reflections are not seen in Figs. (10), (11) and (12).

5. Acknowledgments

We greatly acknowledge the financial support of CAPES and FAPESP. We thank Prof. Máarcio T. Mendonça and Elmer Gennaro for the fruitful discussions.

6. REFERENCES

Anderson, J. D.,1990, Computational Fluid Dynamics - The Basics With Applications, McGraw-Hill.

Bogey, C. & Bailly, C. & Juvé, D., 2000, "Numerical simulation of sound generated by vortex pairing in a mixing layer", AIAA Journal, Vol.12, pp. 2210-2218.

Colaciti, A. K. & Germanos, R. A. C. & Medeiros, M. A. F.,2006, "ON THE VORTEX PAIRING AEROACOUSTICS OF A 2D MIXING LAYER UNDER TEMPORAL DEVELOPMENT", Proceedings of the 11th. Brazilian Congress of Thermal Sciences & Engineering, Vol.11, Curitiba, Brazil, in CD-ROM.

Colonious, T. & Lele, S. K.,2004, "Computational aeroacoustics: progress on nonlinear problems of sound generation", Progress in Aerospace Sciences, Vol.40, pp. 345-416.

Colonious, T. & Lele, S. K. & Moin, P.,1997, "Sound generation in a mixing layer", J. Fluid Mech., Vol.330, pp. 375-409.

Fortuné, V.,2000, "Étude par Simulation Numérique Directe du rayonnement acoustique de couches de mélange isothermes et anisothermes", Thesis, Université de Poitier.

Germanos, R. A. C. & Medeiros, M. A. F.,2005, "Development of a code for a direct numerical simulation of compressible shear flow instabilities", Congresso Brasileiro de Engenharia Mecânica - COBEM 2005, in CD-ROM.

Lele, S. K.,1992, "Compact finite difference schemes with spectral-like resolution", J. Comp. Phys., Vol.103, pp. 16-42.

Lighthill, M. J.,1952, "On the sound generated aerodynamically I. General theory". Proc. R. Soc. Lond. A 211, 564-587.

Mitchell, B. E. & Lele S. K. & Moin P.,1995, "Direct computation of the sound from a compressible co-rotating vortex pair", J. Fluid Mech., Vol.285, pp. 181-202.

Möhring, W.,1978, "On vortex sound at low Mach number", J. Fluid Mech., Vol.85, pp. 685-691.

Möhring, W.,1979, Modelling low Mach number noise. In *Mechanics of Sound Generation in Flows* (ed. E.-A. Müller), pp. 85-96. Springer.

Powell, A.,1964, "Theory of vortex sound", J. Accoust. Soc. Am. Vol.36, pp. 177-195.

Sandham, N. D.,1990, "A numerical investigation of the compressible mixing layer", Phd Thesis, Stanford University.

Sandham, N. D. & Reynolds, W. C.,1991, "Three-dimensional simulations of large eddies in the compressible mixing layer", J. Fluid Mech., Vol.224, pp. 133-158.

Sesterhenn, J.,2001, "A Chracteristic-type formulation of the Navier-Stokes equations for high order upwind schemes", Computers & Fluids, Vol.30, pp. 37-67.

Wang, M. & Freund, J. B. & Lele, S. K., 2006, "Computational Prediction of Flow-Generated Sound", Annu. Rev. Fluid Mech, Vol.38, pp. 483-512.

7. Responsibility notice

The authors are the only responsible for the printed material included in this paper

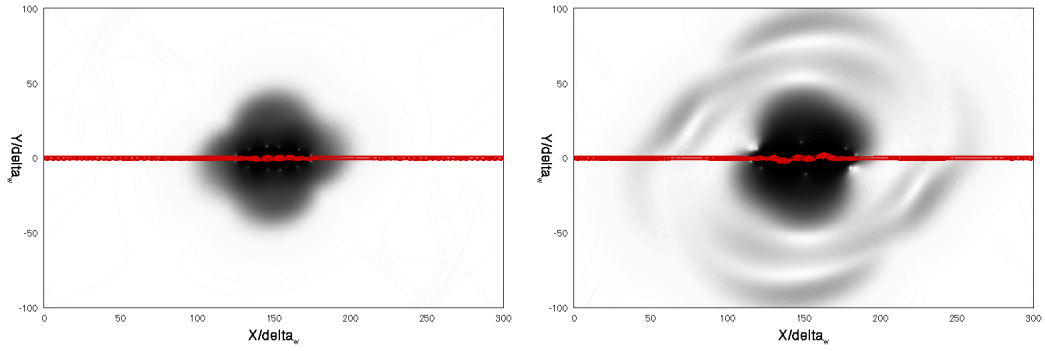

(a) $t = 32.8$ (b) $t = 44.4$

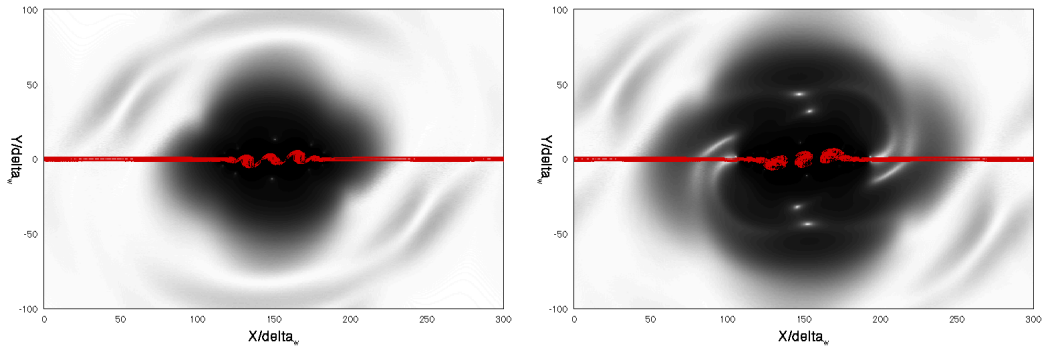

(c) $t = 50.8$ (d) $t = 57.2$

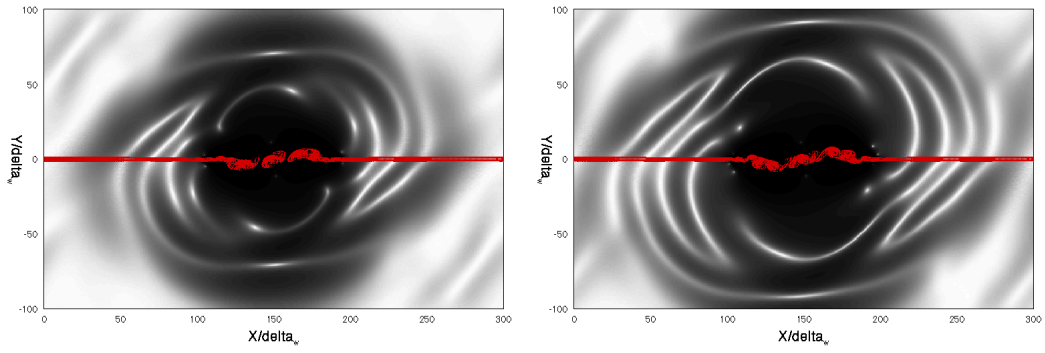

(e) $t = 62.0$ (f) $t = 66.0$

Figure 10. Shaded view of $\log\left(\frac{P}{P_0}\right)$ field and contour plot of the vorticity field for $Ma = 0.2$.

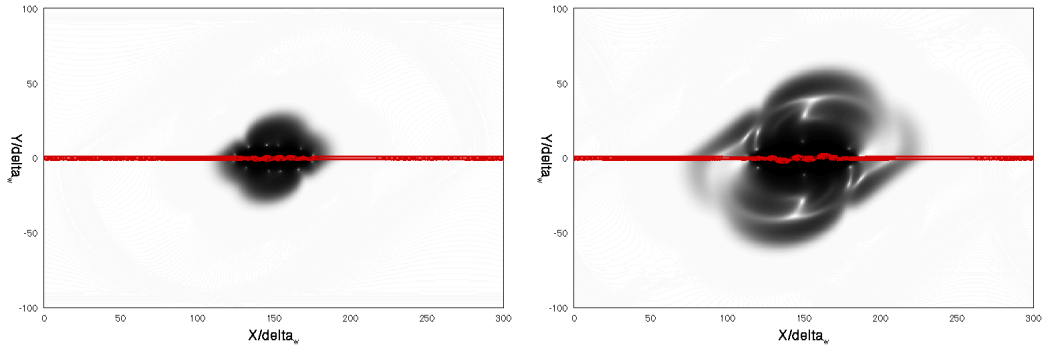

(a) $t = 37.6$ (b) $t = 50.0$

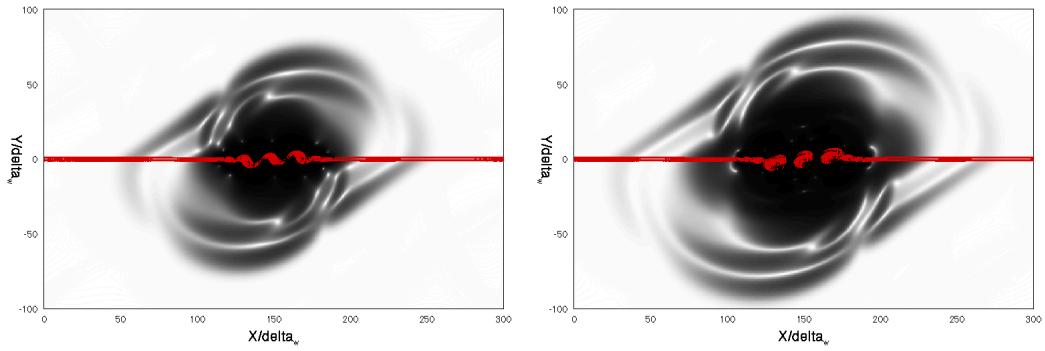

(c) $t = 56.8$ (d) $t = 64.4$

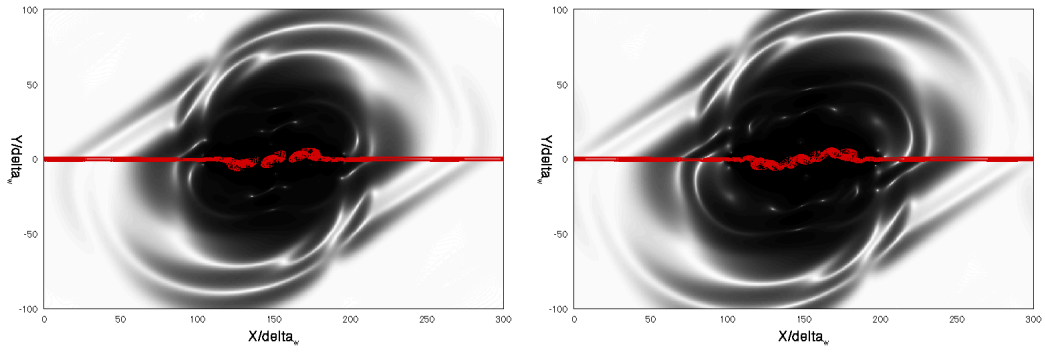

(e) $t = 68.8$ (f) $t = 73.6$

Figure 11. Shaded view of $\log\left(\frac{P}{P_0}\right)$ field and contour plot of the vorticity field for $Ma = 0.4$.

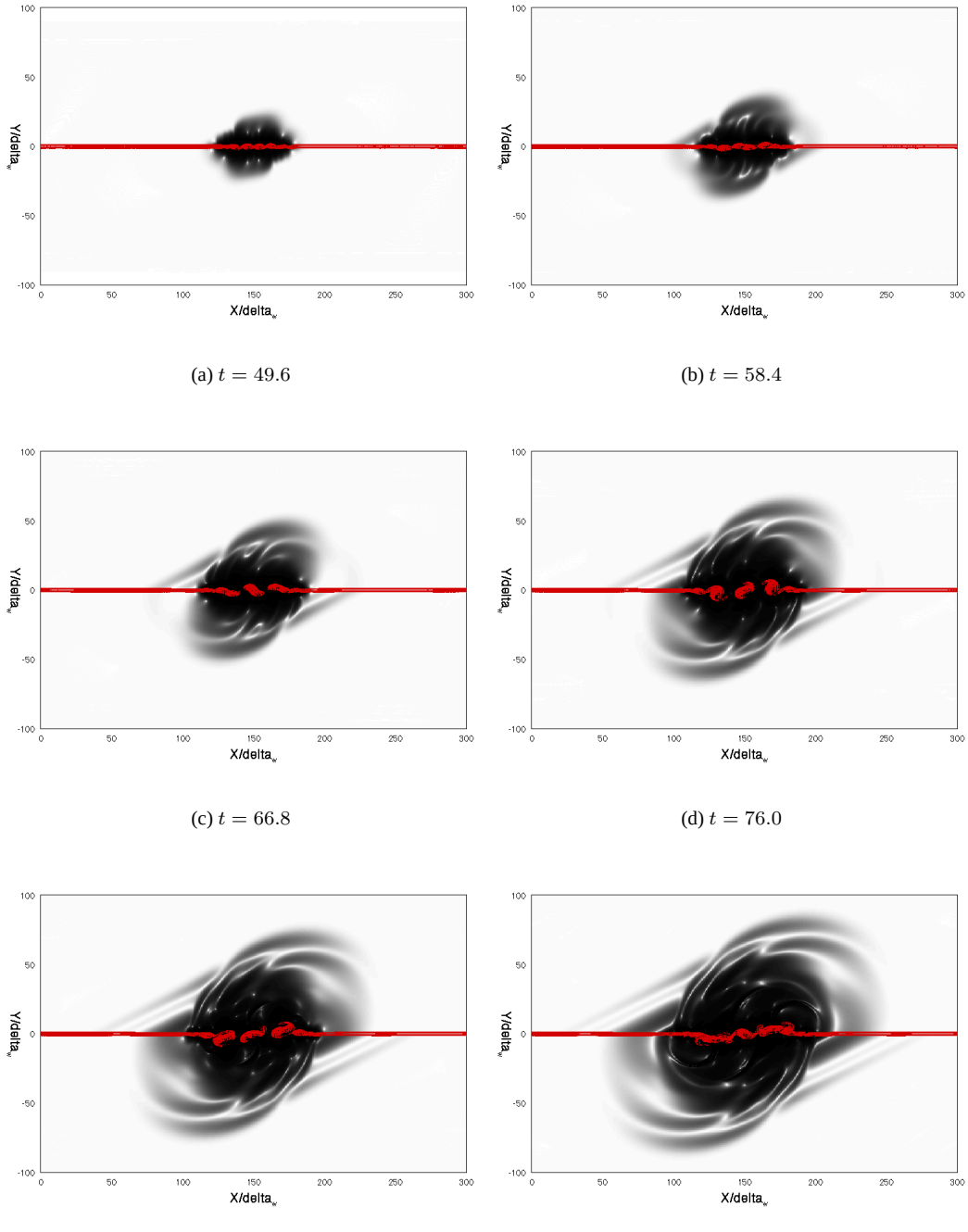

(a) $t = 49.6$ (b) $t = 58.4$

(c) $t = 66.8$ (d) $t = 76.0$

(e) $t = 81.6$ (f) $t = 88.0$

Figure 12. Shaded view of $\log\left(\frac{P}{P_0}\right)$ field and contour plot of the vorticity field for $Ma = 0.6$.